Feasibility Study and System Design for a Spaceborne Along-track Interferometer/Scatterometer

Delwyn Moller[1], Charles Werner[1], Stephen Frasier[2]

November 2, 1998

[1] Delwyn Moller and Charles Werner are with the Radar Science and Engineering section at the Jet Propulsion Laboratory. Contact: moller@muscovy.jpl.nasa.gov

[2] Stephen Frasier is a Professor in the Electrical and Computer Engineering Department, University of Massachusetts, Amherst, MA.

Contents

1 Introduction

Scatterometry is a well established and heavily utilized technique that routinely provides vector wind measurements over the ocean with resolution cells on the order of 60 kilometers on a side [1, 2, 3]. Despite the maturity of this field, the 'ambiguity problem' (whereby the wind direction measurements can suffer a large directional ambiguity) remains a source of error in scatterometry [4, 5, 6]. This feasibility study will investigate a system solution to the ambiguity problem by measuring an additional quantity: the ocean surface Doppler velocity.

For moderate incidence angles, ocean electromagnetic backscatter is generally dominated by a resonant phenomena known as Bragg-scattering. At the frequencies considered for spaceborne systems the Bragg-resonant waves are highly sensitive to the wind-direction. Two major (and usually dominant) components of the Doppler velocity measurement are the phase-speed of the Bragg-resonant waves and the surface wind-drag, both of which follow the wind direction. Therefore the surface velocity can be used to directly infer the wind direction.

Figure 1 summarizes the system concept, its data products and scientific motivation. In addition to resolving the ambiguity problem, the velocity measurements can be used to derive ocean surface currents. In particular, airborne along-track interferometric synthetic aperture radar (ATI-SAR) systems have demonstrated success in imaging surface ocean currents with relatively fine spatial resolution [7]. This report evaluates the potential of a spaceborne along-track interferometric SAR with squinted geometries to make vector measurements of (unambiguous) ocean winds and velocities with km-scale resolution (much finer than the 60km resolution cells typical of conventional spaceborne scatterometers). Measurements at these resolution will provide useful data for coastal monitoring and characterization and enable observation of small-scale eddies and possibly signatures of atmospheric boundary turbulence.

Furthermore, a combined scatterometer/interferometer has important implications for air-sea interaction studies. The exchanges of heat and water at the air-sea interface control a key feedback loop between the atmospheric and oceanic circulations. Toward understanding this process, the measurement of ocean surface wind stress is identified in the Mission To Planet Earth (MTPE) Science Research Plan as one of the key missing observations for better understanding long-term climate change and air-sea interaction processes. The synergy of coincident ocean surface current and wind velocity measurements will help address this shortfall.

In this report Section 2 summarizes the scatterometry and along-track interferometric measurement techniques. This review illustrates fundamental relationships and issues that govern or limit a system design for these applications. We also discuss the use of SAR as a scatterometer. The concept of a SAR-based scatterometer for higher resolution measurements has been successfully demonstrated in the works of [8, 9, 10] and is identified in the 1997 MTPE Capability/Technology Needs Assessment as the future direction of scatterometry systems.

Section 3 presents a nominal system design. At its essence, this design is one of an unfocused ScanSAR with squinted geometries. The fore and aft squints provide azimuthally diverse measurements for wind and velocity vector retrieval. We use an unfocused aperture since the coherent length of the synthesized array is short enough that there is little advantage to focusing. In order to gain swathwidth, we scan in elevation with no loss of resolution because the ocean decorrelation time is much shorter than the maximum aperture synthesis

time. Section 4 predicts the performance of the nominal design in terms of the signal to noise ration (SNR), and phase measurement accuracies.

The design presented in this document is initial only and there are a number of alternatives to parameter choices. As such Section 5 discusses alternate design choices and their implications in terms of configuration and measurement accuracies. Finally, Section 6 makes recommendations for the further development of this concept. In particular we recommend a series of focused experiments from an airborne platform.

Spaceborne Along-track Interferometer/Scatterometer

Investigate the feasibility of combining along-track interferometry and scatterometery

- provide vector surface velocity measurements in addition to surface wind vectors
- yield a system solution to the scatterometric 'ambiguity' problem

Science Applications

◆ Eliminating the age-old ambiguity problem will greatly enhance the scatterometric data value

◆ Coincident wind and surface velocity vectors a unique data set for air-sea interaction research.

◆ Measurement scales useful for observation of atmospheric turbulence signatures in the ocean

◆ Surface currents extracted from velocity vectors provide data for upper-ocean circulation studies.

Scatterometry Wind Vectors (NSCAT)

from http://winds.jpl.nasa.gov
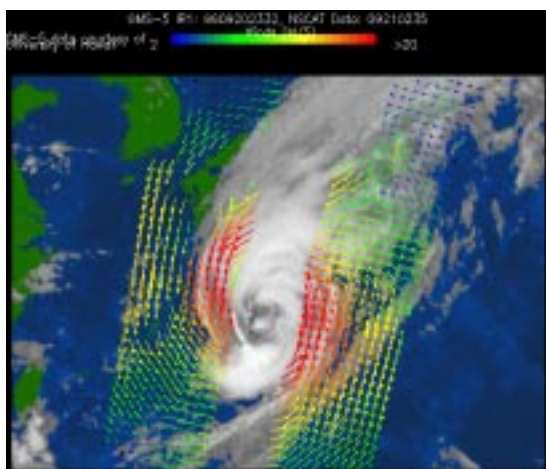
Measurement Goals

◆ azimuth resolution: O(1km)

◆ minimum swathwidth: 200km

◆ wind-speed accuracy: 2m/s

◆ wind-direction accuracy:
20 deg. unambiguous

◆ velocity measurement accuracy:
O(10cm/s)

Along-track Interferometric Surface Velocity Vectors

AIRSAR velocity vector image courtesy Ernesto Rodriguez

Figure 1: System and measurement concept.

2 Summary of Measurement Techniques

2.1 Summary of Scatterometry

A scatterometer calculates the radar cross section, σ_0 from the radar range equation

$$\sigma_0 = \frac{(4\pi)^3 R^4 L P_s}{P_t G^2 \lambda^2 A} \tag{1}$$

where R is the slant-range, P_t is the transmitted power, P_s is the (estimated) received signal power, G is the ant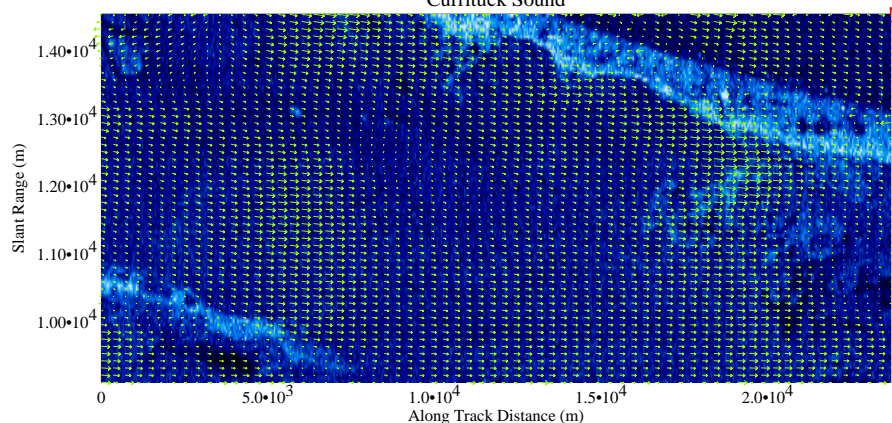enna gain, L is the system losses, A is the effective illuminated area and λ is the transmitted wavelength. Satellite-based radar measurements of σ_0 over the ocean surface translate via empirical formulae into wind speed and direction [1, 2, 3]. This relationship exists because the wind roughens the water surface via the production of capillary-gravity waves [11, 12] which in turn, effectively backscatter radar signals via Bragg scattering for incidence angles between $20° - 70°$ [13]. Bragg scattering [14] is a resonant effect that occurs when the following relationship is true:

$$\lambda = 2\lambda_B sin(\gamma) \tag{2}$$

where λ is the radar wavelength, λ_B is the Bragg-resonant ocean wavelength and γ is the incidence angle. When this condition is true, the backscattered returns add in phase, thus creating the resonant effect.

2.1.1 Azimuthal Dependence of Backscatter

The azimuthal variation of backscatter at moderate incidence angles can be described (to first order) by [15]:

$$\sigma_0 = A + Bcos\phi + Ccos2\phi \tag{3}$$

where ϕ is the angle between the upwind direction and the radar look direction. The coefficients A, B and C are functions of the wavelength, angle of incidence, polarization and windspeed. The $cos(2\phi)$ dependence of the backscatter is primarily responsible for the difficulties in obtaining unique estimates of the wind vector from σ_0. Equation (3) has a multivalued inverse, and as such measurements of σ_0 are required from several different azimuth angles in order to estimate the wind vector. The SeaSAT scatterometer provided measurements of σ_0 at two different azimuth angle separated by $90°$. NSCAT improved on this with σ_0 measurements from three distinct azimuth angles with separations of $65°$ and $90°$ respectively. However, because the number of observation angles are small, There may be several wind vectors that give rise to the same set of σ_0 observations or ambiguities. The problem of ambiguity removal for scatterometry has been studied extensively and research continues today for further improvement [4, 5, 6]. This report details a system concept that delivers a measurement-based solution to the ambiguity problem.

2.1.2 Measurement Accuracies

The following measurement goals were established for the NSCAT mission:

wind speed accuracy	2m/s (rms)	3-20m/s
	10%	20-30m/s
wind direction	20°	3-30m/s
(rms- closest ambiguity)		
spatial resolution	25km	σ_0
	50km	wind cells
swathwidth	600km	(one-side)
(giving 2-day repeat coverage for orbit)		

We use these goals as a guideline for our system measurement goals.

2.2 Summary of Along-track Interferometry

An ATI-SAR employs two SAR antennas spatially separated in the along-track direction to yield two complex SAR images that are separated by a time lag equal to the antenna separation divided by the platform velocity (for the configuration where one antenna transmits and receives, then the other transmits and receives). The covariance of the two images is an interferogram, the magnitude of which is akin to a conventional SAR image while the phase contains Doppler velocity information.

Doppler velocity measurements are derived from the phase of the covariance of the backscattered field evaluated at a lag time, Δt,

$$\phi = \arg C(\Delta t) \tag{4}$$

where $C(\tau)$ is defined as

$$C(\Delta t) = < I(t)I^*(t + \Delta t) > . \tag{5}$$

$I(t)$ is the complex backscattered field at time, t, evaluated at each image pixel. The operator $< . >$ represents a coherent integration several independent looks to reduce the variance of the fading statistics. Assuming Δt is less than the decorrelation time of the echo signal at the transmitted frequency, the phase of $C(\Delta t)$ is directly proportional to the mean Doppler frequency [16]. The phase is converted to a velocity through

$$v = \frac{\lambda}{2 \sin \theta_i} \frac{\phi}{2\pi \Delta t}, \tag{6}$$

where λ is the radar wavelength and θ_i is the incidence angle.

2.2.1 Components of Surface Velocity Measurements

An ocean surface Doppler velocity measurement is comprised of several contributing factors,

$$v = U_c + U_d + v_o + v_b \tag{7}$$

where U_c represents a bulk water current due to a number of driving forces including, but not limited to, tidal currents and wind-driven flow. U_d is the wind drift current, v_o is the orbital velocity of the gravity waves, and v_b is the net velocity reported due to the phase velocities of Bragg-resonant waves. Bragg theory predicts a radar echo power proportional to the spectral density of radially travelling (i.e. both advancing and receding) resonant waves [13]. The net Doppler velocity due to these waves is a power-weighted combination of their oppositely signed phase velocities.

We consider a radial surface current, U_s, to consist of the first two terms of (7), that is $U_s = U_c + U_d$. Thus, to extract the surface current from an interferometric or Doppler velocity measurement the contributions of v_o and v_b must be extracted. In general, it is assumed that wave-orbital velocities average to zero over a number of wave periods. As is discussed later in this section, coupling between the wave orbital velocity and backscattered power bias the average velocity and therefore the surface current estimate. The extent of this bias is sensitive to the radar orientation and the processing approach used.

2.2.2 Bragg Phase-speed and Unambiguous Wind Direction

The phase-speed of the Bragg-resonant capillary-gravity waves is given by

$$v_p = \sqrt{\frac{g}{|\boldsymbol{k}|} + \frac{\tau_s |\boldsymbol{k}|}{\rho}}, \tag{8}$$

where g is gravitational acceleration, τ_s is surface tension, ρ is water density and $\boldsymbol{k}$ is the wavenumber of the Bragg-resonant waves [17]. Equation 8 is at a minimum for $v_p \approx 0.23 ms^{-1}$ ocurring at a Bragg-resonant wavelength of approximately 1.5 cm. For Bragg-resonant waves greater or less than this v_p will be higher.

The velocity measured by the radar is dictated by the ratio of the spectral densities of advancing and receding waves within the resolution cell,

$$v_b(\theta) = \alpha(\theta)v_p - (1 - \alpha(\theta))v_p = [2\alpha(\theta) - 1]v_p \tag{9}$$

where α and $1 - \alpha$ represents the respective proportions of approaching and receding Bragg-resonant wave spectral density contributing to the radar echo. In general, at the transmit wavelengths of interest, one can assume the Bragg waves follow the wind direction. Therefore when looking directly upwind $\alpha = 1$ and $v_b = v_p$. Similarly, looking downwind $\alpha = 0$ and $v_b = -v_p$. Off the wind axis however, it is difficult to determine a value for v_b since α is unknown. Given that v_p is a strong component ($> 0.23 ms^{-1}$) of the total measured velocity, coupled with the fact that, in most instances the surface current follows the wind-direction (strong tidal flows in coastal regions or river inlets may be an exception to this) a surface velocity vector provides an unambiguous indicator of wind direction.

2.2.3 Modulation Transfer Function Effects

To extract the surface current from radar imagery, one approach is to assume that observed Doppler velocity modulations due to wave orbital velocities average to zero over a number of wave periods. This is rarely the case, however. First, fluid particles do not generally follow closed orbits, yielding a small net velocity in the wave direction (Stokes drift). From the radar measurement perspective, this may be treated as another component of the surface current. Second, it is known from numerous measurements of the radar Modulation Transfer Function (MTF) [18, 19, 20] that coupling between the amplitude and phase responses of the microwave return due to both geometrical and hydrodynamic sources can lead to a bias in the mean Doppler velocity. The bias can be explained in terms of the MTF, as the portions of the long waves tilted towards the radar contribute more power than other portions biasing the mean velocity toward the higher power regions of the waves. This effect is most pronounced when looking into the wave-field, where the approaching regions of the gravity waves will be weighted more heavily than the receding regions, thus incurring a positive velocity bias. In a later section we obtain rough estimates of the magnitude of this potential bias by reviewing the available literature on this subject.

2.3 SAR as a Scatterometer

It is notable that there are several examples of applying scatterometer algorithms to SAR ocean images to infer the local wind-field [8, 9, 10] with often surprisingly good results. Wackerman [8] used scatterometer algorithms to calculate local wind-speeds in SAR images, which when compared with in situ data was within ± 1.2m/s and $\pm 19°$. Similarly Vachon and Dobson [9] compared SAR and ship-based in situ wind measurements. For wind speeds between 3 and 12m/s the remotely sensed winds were within ± 1.2m/s using CMOD4. In this instance, they used in situ wind direction measurements as input to the wind-retrieval algorithm. If they used SAR-inferred wind directions instead, the wind-speeds were within ± 3 m/s of the in situ measurements (for CMOD4).

The successful application of scatterometer algorithms to SAR images requires an accurate estimate of the wind direction. As a further illustration of this, Lehner [10] found that a $10°$ error in wind direction estimate produced up to a 25% error in wind-speed (again using CMOD4).

The system proposed here provides a significant improvement for SAR-based scatterometery through the measurement of back-scatter from distinct azimuthal directions. Furthermore, the along-track interferometric measurements provides a further basis for establishing the wind-direction. Based on the aforementioned findings [8, 9, 10] and the system improvements we propose, we anticipate that the system outlined in this document will be capable of meeting the wind-retrieval accuracy goals.

3   Nominal System Design

The nominal interferometer/scatterometer design consists of a Ku-band unfocused ScanSAR with squinted beams for azimuth diversity and an along-track separation for velocity measurements. We selected Ku-Band because there is a wealth of scatterometer experience in this band, and because out of the frequency bands considered (Ku-, C- and L-band) Ku-band is the most appropriate for a single space-craft configuration. Section 5 discusses the implications of translating the system design to a lower frequency. In particular a dual space-craft configuration system at L-band is discussed.

3.1   Measurement Goals

We identified the following measurement goals:

- azimuth resolution O(1km)

- coverage (swathwidth): minimum 200km (one-side)

- velocity measurement accuracy: O(10cm/s)

- Wind-speed measurement accuracy: 2m/s (winds between 3-20m/s)

- Wind direction measurement accuracy: 20° unambiguous

The wind field measurement goals were chosen to be generally consistent with the NSCAT mission goals although the swathwidth goal is less stringent. An important distinction is that the wind-direction accuracy is specified as unambiguous. The resolution goal is ambitious, but is aligned with MTPE future goals for a SAR-based scatterometer. The enhanced resolution will enable useful measurements of coastal wind-fields, opening up an entirely new field of observation and analysis, in addition to allowing observation of small-scale eddies. The velocity measurement accuracy goal is also an ambitious one, but acheivable as later analysis will show.

3.2   Design Overview

3.2.1   Squinted Geometry and Beam Configuration

Figure 2 shows the antenna illuminations assumed in this initial design. For a configuration looking from both sides of the spacecraft there are a total of eight-beams, composed as two sets of four separated in the along-track dimension by a physical baseline B.

The squinted viewing geometries in Fig. 2 will enable us to combine radial velocities to infer a surface velocity vector. With both forward and aft squints we are assured that at least one squint direction will not be cross-wind where the ratio of approaching to receding Bragg-waves is unknown. By looking on both sides of the spacecraft we double the total swath-width.

3.2.2   Focusing and Scanning Configuration

An important limitation of using SAR over the ocean is the scene correlation time, which ultimately determines the along-track resolution. At Ku-Band the correlation time is quite short; we assume less than 10ms. In this case, at an average space-craft velocity of 7km/s

Plan view of proposed beam configuration.

ϕ_{sq}

Vsp

B

◆ A duplicate set of beams, separated by baseline B, result in temporally disparate measurements of the scene from which the surface velocity can be inferred.

◆ Fore and aft squinted beams on both sides of the spacecraft

    - different azimuth views can be used to measure a velocity vector
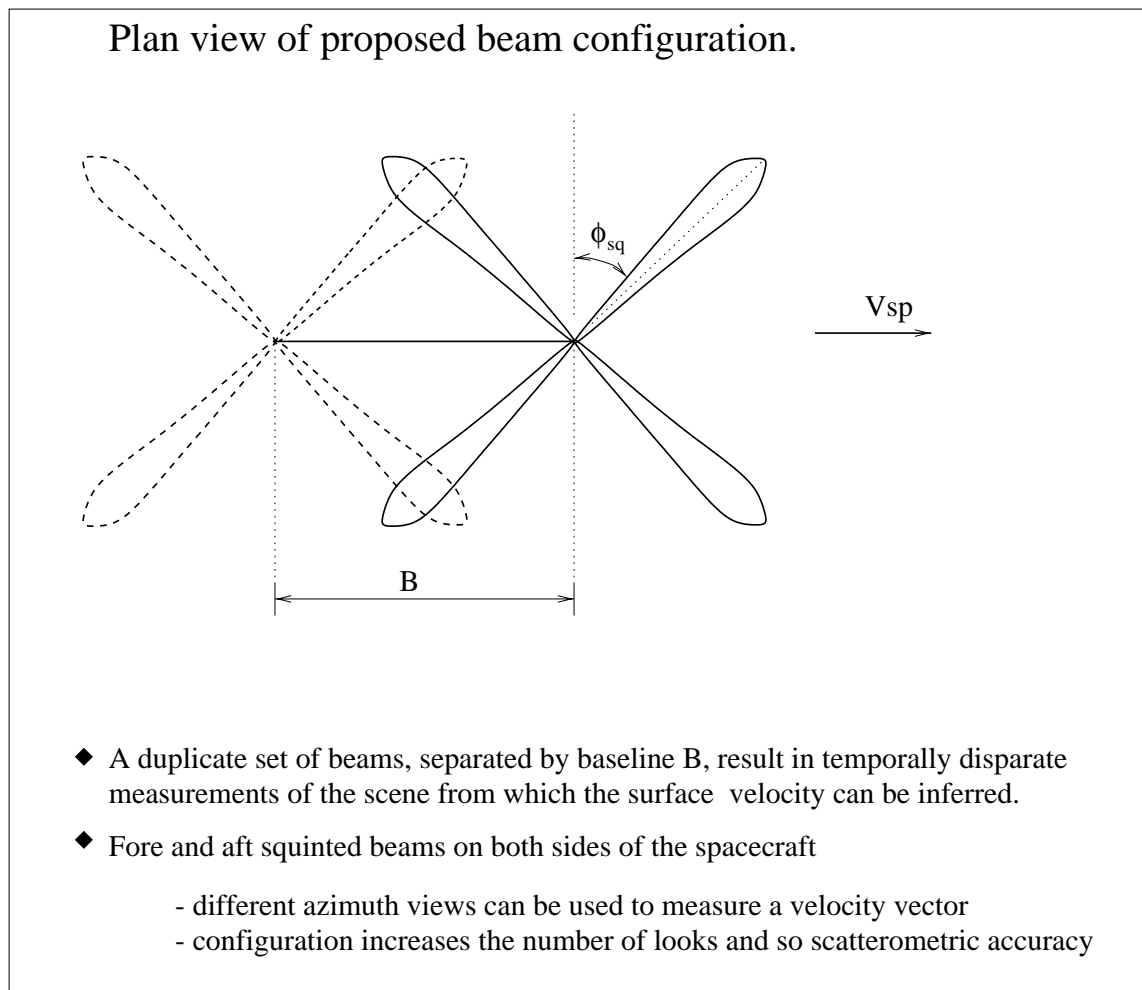   - configuration increases the number of looks and so scatterometric accuracy

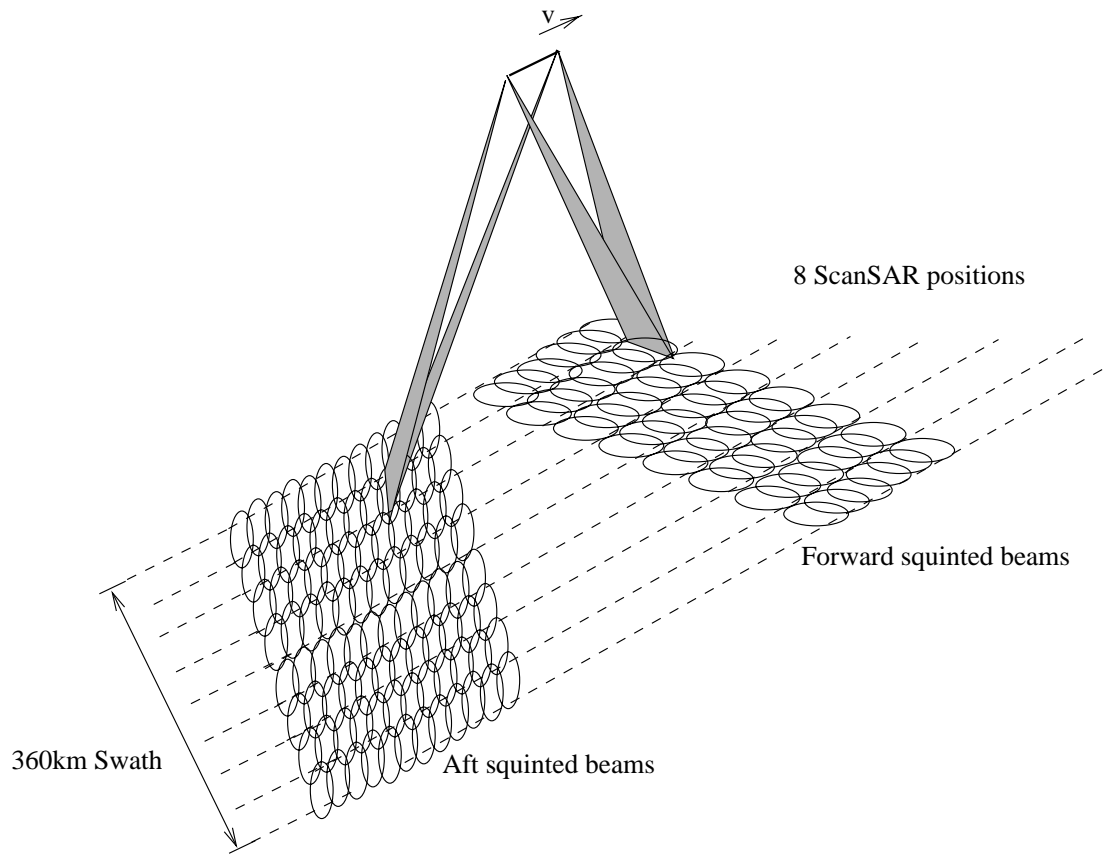Figure 2: antenna beam viewing geometry

Figure 3: ScanSAR configuration (illustrated for one-side only). There are eight subswaths in the nominal design yielding a swathwidth of 360km.

the maximum correlated synthetic aperture length is 70m; much shorter than the fully focused length for the antenna sizes under consideration. Even with the shortened aperture, the along-track resolution is approximately 300m (4-look) and so still well within our goals. Given this fundamental constraint, the system design we propose is an unfocused ScanSAR, conceptually illustrated in Fig 3. By scanning in elevation within the focused aperture length we gain swath-width. The current design has eight subswaths yielding a total swathwidth of 360km on one side.

3.2.3   Pulse Timing and Physical Baseline

Because we are designing (in this instance) a single space-craft system, we wish the physical baseline to be as short as possible. The transmit/receive pulse sequence between the fore and aft antennas is a key issue. Ignoring the squinted geometries momentarily, if we transmit on a fore antenna and receive on both fore and aft simultaneously, the effective baseline between the two is half the physical baseline because the relative phase-center is half-way between the two antennas. However if we sequentially transmit fore, receive fore, transmit aft receive aft the effective baseline is that of the physical baseline. For a single spacecraft configuration where we want to minimize the physical baseline this is the mode to use. Figure 4 shows this pulsing sequence. The solid lines indicate the transmit pulse and receive echo on a given antenna. The dashed lines shadow the transmit/receive events on

the alternate antenna. Note that the effective PRF is twice that of the actual PRF for each antenna.

3.3   Fundamental Parameter Selection

The following table itemizes system parameters that are common over all the subswaths.

Common Ku-Band Radar System Parameters

Altitude	770 km	Antenna Length	7 m
Velocity	7470.01 m/s	Antenna Width	.5 m
Center Frequency	13.8 GHz	Noise Temperature	800 K
Bandwidth	1 MHz	ISLR	-15 dB
Transmit Peak Power	15 W	System Losses	-4.5 dB
Pulse Duration	50 micro-s	Oversampling factor	1.2
Proc. Doppler Bandwidth	100 Hz	Radius of Curvature	6378 km
Bits per Sample	4		

Some of the key design decisions which led to the selection of these and other parameters are summarized below:

1. The small processing bandwidth constrains the synthetic aperture length to approximately 70m (at a spacecraft velocity of 7km/s). The fully focused aperture length is over 2.5 km for a 7m antenna; therefore over 30 subapertures are possible.

2. The nominal design utilizes eight subswaths. Scanning each of these in elevation yields a swathwidth of over 350km swath (one side of the space-craft only). It is possible to increase the swath even further, although this may require more transmit power.

3. We chose a transmit power of 15W which is low enough that a Ku-Band solid-state amplifier can supply this. It may be possible to increase the power through increasing the number of solid-state transmit-receive (T/R) modules.

4. For an antenna length of 7m the azimuth ambiguities across the subswaths were low (more than 30dB down at the subswath boresights); therefore it may be possible to shorten the antenna further.

5. Despite the low Doppler bandwidth an (effective) pulse-repetition frequency (PRF) of over 2kHz was chosen for all the subswaths. This PRF is chosen for colocating the returns from two temporally separated antennas (the temporal separation of the antennas will be O(2-4ms)).

Single Squint Transmit/Receive Pulse Timing (Not to scale)

Fore Antenna

T

Transmit pulse

Receive echo from N pulses ago

Aft Antenna

T
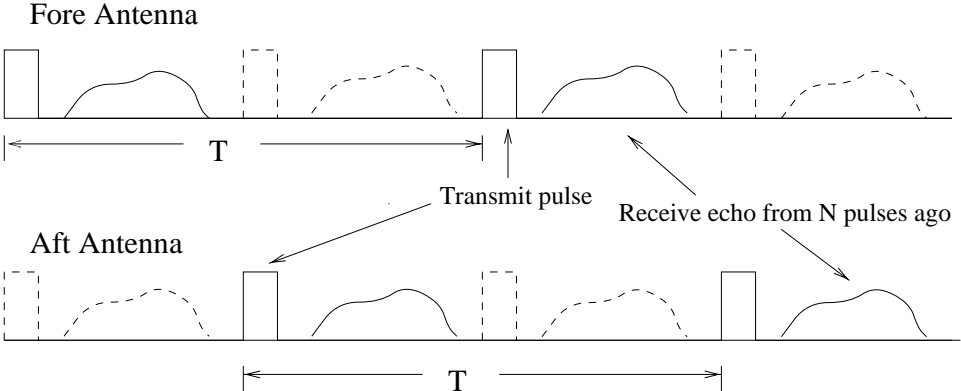
Individual PRF =1/T
Effective PRF =2/T
Effective Baseline = Physical Baseline

Figure 4: Transmit and receive pulse timing between fore and aft antennas for along-track interferometry.

4 System Performance Summary

This section summarizes the performance of the system across all subswaths and discusses possible design tradeoffs. For more insight Appendix A considers one subswath in detail, while Appendix B shows the fact sheets for each subswath individually. Refer to Appendix C for details on parameter definitions and equations used.

4.1 SNR Over Subswaths

The data swath corresponds to look angles ranging from 20.2° to 39.6° (incidence angles ≈ 23° to 45°) resulting in a swathwidth of over 350km. These incidence angles are in the Bragg-scattering regime.

Figures 5 shows the signal and noise levels across the subswaths. One can see that the SNR ranges from over 20 dB at Swath 1 boresight to just a few dB at the swath edges of the far subswath. Even for the near swaths we will likely want to average more looks to increase SNR and lower the phase noise. The following section addresses these issues in detail. The 4-look azimuth resolution is ≈ 300m and the ground range resolution ranges from ≈ 190m to ≈ 320m. Therefore additional range and along-track averaging can occur without jeopardizing our resolution goal.

To further characterize the performance of this system, we have computed the SNR-equivalent σ_0 for particular values of Signal-to-Noise Ratio (SNR). This quantity is defined as the value of the scattering cross-section, σ_{SNR}, where the SNR achieves a particular value. Figure 6 shows σ_{SNR} as a function of swath. One can observe a gradual increase in the σ_{SNR} as the subswaths increase in range (and incidence angle).

4.2 Interferometric Phase Sensitivity Analysis

4.2.1 Correlation Time

The choice of interferometric baseline hinges on sufficient correlation between the two successive looks at the surface. For this, we need some estimate of the correlation time of scattering from the ocean surface. This is known to be a function of both illuminated area and the "lifetimes" of Bragg-resonant scatterering facets. Plant et. al. [21] has shown that lifetime effects are important only for relatively small illuminated areas (up to a few m^2). For large illuminated areas, it is the rms velocity spread within the illuminated area that dictates the Doppler bandwidth and hence the correlation time. The rms velocity spread is essentially the range of orbital velocities of the larger-scale gravity waves that are included within the field of view. The rms orbital velocity is a function of sea-state. In general, values between 0.50 m/s (Plant's observation) and 1 m/s are typical. At Ku-band, assuming Gaussian Doppler spectra, these yield decorrelation times, τ_c, of approximately 10 ms and 5 ms respectively, where $\rho(\tau_c) = e^{-1}$. Under calm conditions, τ_c may be as high as 20 ms. For the remainder of this report, we will assume $\tau_c \approx 7$ ms.

To obtain meaningful interferometric measurements, the delay, τ, between two looks at the surface needs to be less than τ_c. The value of τ determines the unambiguous Doppler velocity interval according to

$$-\frac{\lambda}{4\tau} < v_D < \frac{\lambda}{4\tau}. \tag{10}$$

For example, a $\tau = 3$ ms lag provides well correlated looks and an unambiguous Doppler velocity range of ±1.8 m/s.
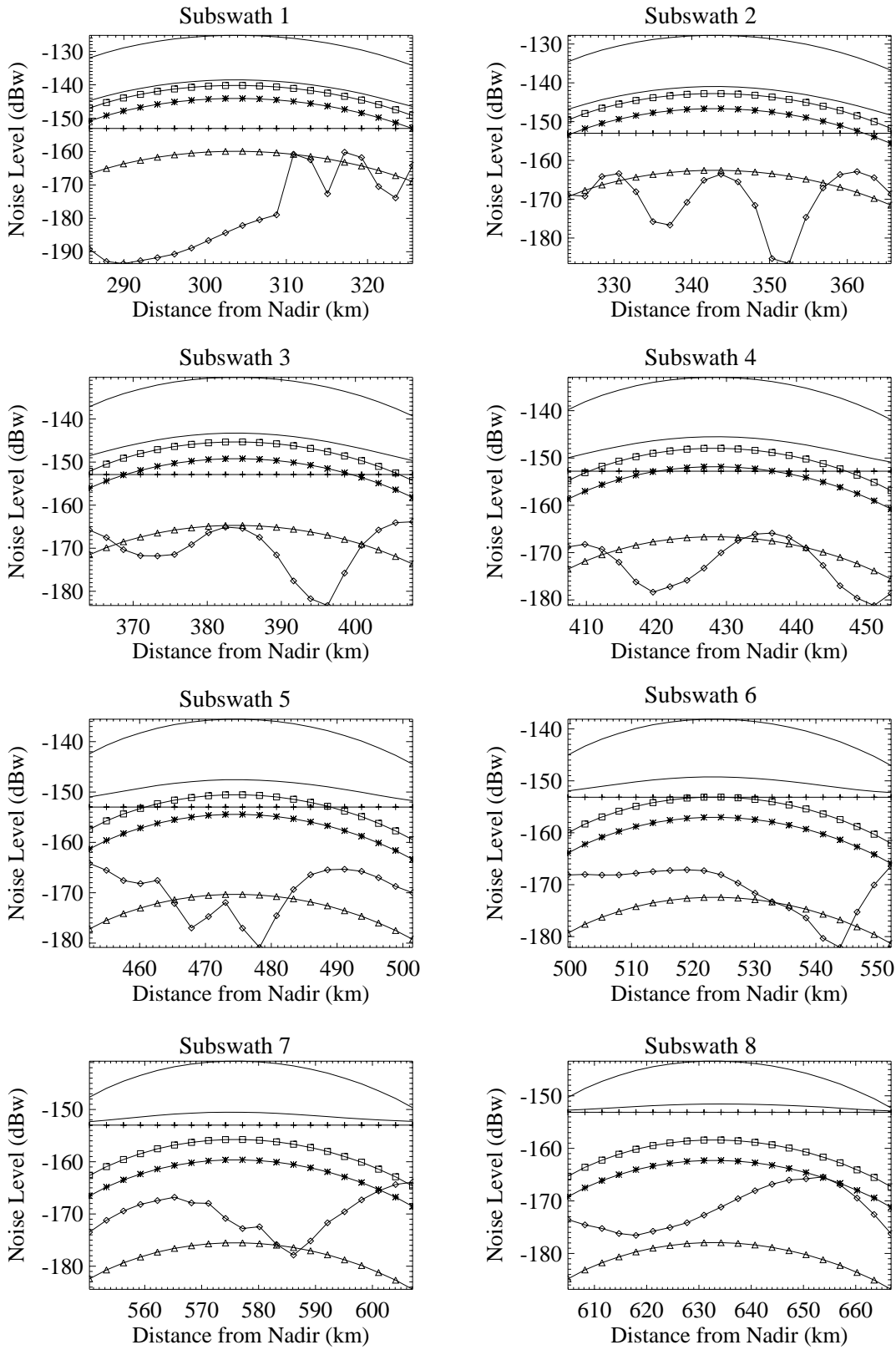
Figure 5: Components of the noise level compared to the signal level for each subswath in this system. Plotted are: signal level (thin line), total noise (thick line), thermal noise (crosses), quantization noise (asterisks), range ambiguity level (diamonds), azimuth ambiguity side-lobe ratio (AASR) (triangles) and integrated side-lobe ratio (ISLR) (squares).
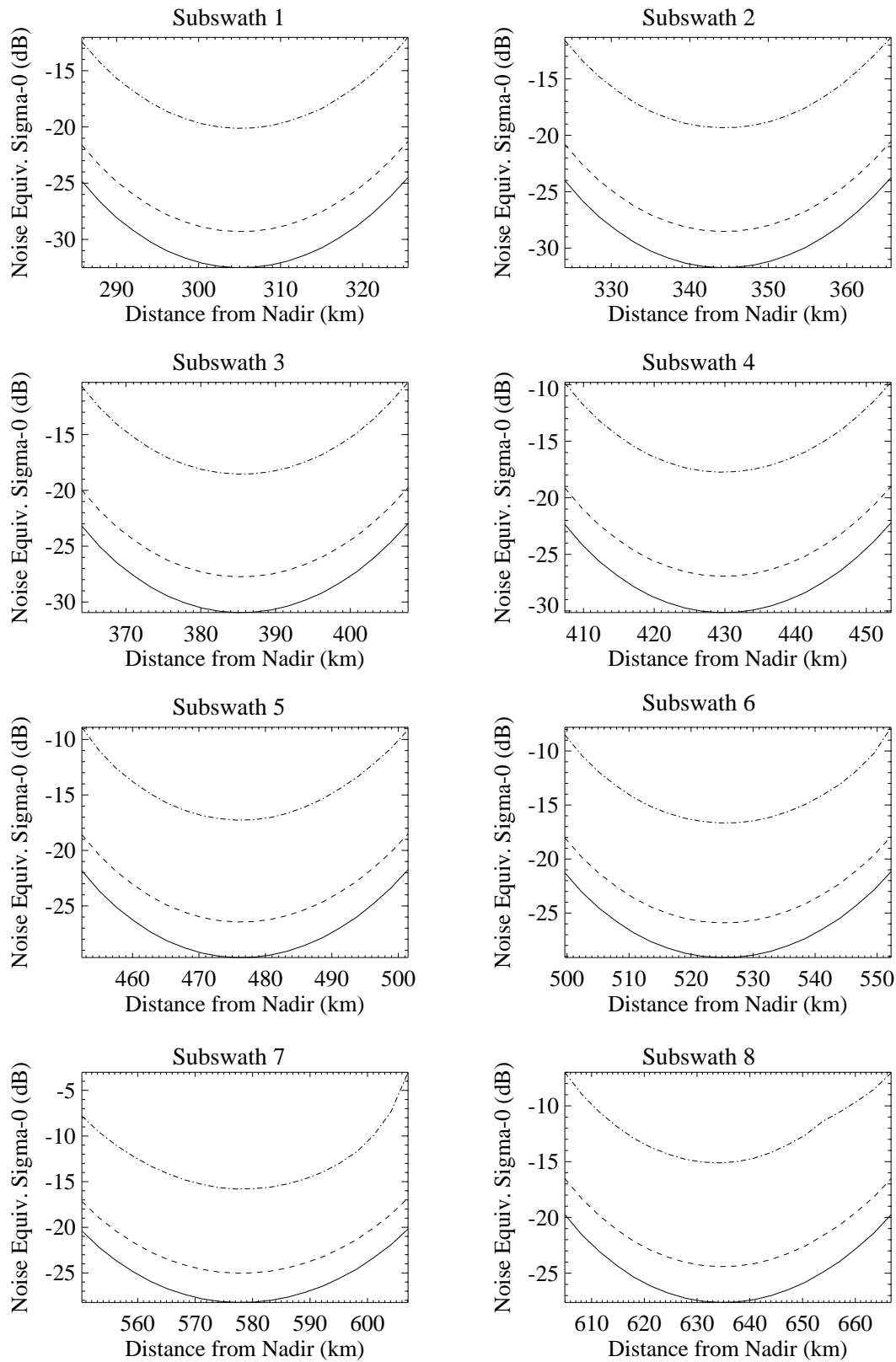
Figure 6: Noise-Equivalent σ_0 plotted as a function of distance along the subswaths. The thick line is for SNR = 0 dB; the dashed line is for SNR = 3 dB and the dash-dot line for 10 dB.
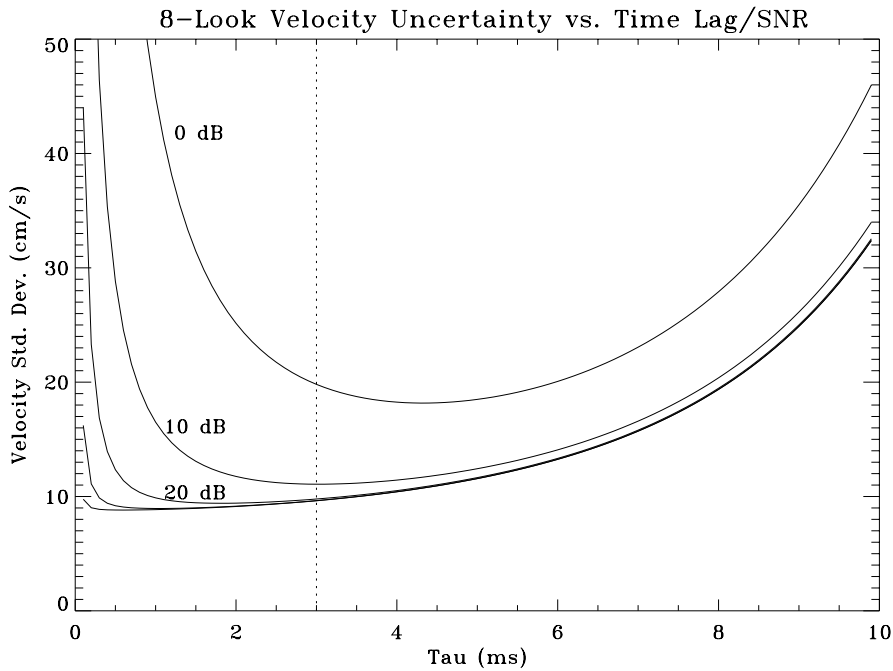
Figure 7: Tradeoff between SNR and decorrelation effects for interferometric measurements.

4.2.2 Signal-to-Noise Ratio

For the purpose of interferometry, our primary interest in signal-to-noise ratio (SNR) is on its effect on phase estimates. Miller and Rochwarger [16] provide an asymptotic formula relating uncertainty in differential phase measurements to the SNR and the correlation coefficient, $\rho(\tau)$. Expressed in terms of Doppler velocity uncertainty, σ_v, it is

$$\sigma_v = \frac{\lambda}{2} \frac{\sqrt{\rho^{-2}(\tau)(1 + SNR^{-1}) - 1}}{\sqrt{2N} 2\pi\tau}, \tag{11}$$

where 2N is the number of independent pairs (or "looks") used in the estimate. Figure 7 plots this function for various SNRs for eight independent looks. Here we have assumed a correlation function of the form

$$\rho(\tau) = \exp\left(-\left(\frac{\tau}{\tau_c}\right)^2\right) \tag{12}$$

where $\tau_c = 7$ ms, the coherence time of the signal.

The figure illustrates two important points. First, the estimate is nearly optimum, achieving minimum variance, for SNR of about 20 dB (as observed by Carande [22]). There is little reason to design for much better SNR than this, and in fact, a SNR of 10 dB is also quite close to optimum. Second, for a given SNR, there is an optimum choice of τ, providing the best tradeoff between the competing effects of noise and decorrelation. For SNR between 10 and 20 dB, this minimum occurs for τ between 2 and 4 ms. Note that this behavior holds regardless of the value of N since it divides the entire expression.

Equation (11) is an asymptotic formula for phase uncertainty (large N implied). For a single-look at high SNR, the uncertainty of the mean velocity is essentially determined by the inherent velocity spread of the scatterers providing the echo. Middleton [23] provides a

rather complicated formula for the pdf of phase differences for bandpass singles appropriate to this problem. This served as a model for Chapman's phase statistics study [24]. Computing the standard deviation of the distribution yields an uncertainty of nearly 60 cm/s for a single look with no along-track (SAR) processing of the signal. The simple unfocused SAR processing that accumulates echoes over the coherence time prior to cross-correlation does not significantly reduce the standard deviation since echoes obtained within the coherence time are, by definition, correlated. Improvements in this estimate come from averaging multiple *independent* looks.

4.2.3 Multilook Averaging

It has been shown [25] that for scattering from the ocean surface, the spatial resolution that can be achieved using synthetic aperture techniques is dictated not by the available integration time due to the antenna beamwidths, but by the coherence time of the surface,

$$r_a = \frac{R\lambda}{2v_p\tau_c}.$$ (13)

Thus, it makes little sense to coherently integrate for much longer than τ_c since no focusing gain is obtained. Since τ_c is quite short, the dimension of the synthetic aperture is small. At 7 km/s, $2v_p\tau_c \approx 100$ m. The far-field of this latter aperture begins about 10 km from the (synthetic) antenna, hence no focusing of the aperture is necessary to achieve optimum resolution.

Because individual patches of surface are illuminated by the antenna for much longer than the coherence time, several independent looks at the surface are available. An approximate value for the number of available looks is given by the ratio of the time a given resolution cell is illuminated by the antenna to the coherence time, $N_L = T_{ill}/\tau_c$. If a ScanSAR approach is to be used, N_L should be divided by the number of subswaths, N_s. Subsituting for T_{ill}, we obtain

$$N_L = \frac{R\lambda}{N_s D v_p \cos\theta_s \tau_c}$$ (14)

where R is slant range, D is the antenna physical aperture, v_p is the platform velocity, and θ_s is the squint angle. For Subswath-4 given the antenna parameters chosen, N_L is about 10. Thus the anticipated 8-look phase sensitivity shown in the plot is a reasonable first guess for the precision of the measurement.

4.3 Squint Geometry

4.3.1 Effect on Doppler

The large forward and aft squint angles proposed for this sensor will impart large Doppler shifts on echo signals due to the component of the satellite's velocity vector in the direction of the radar beam. Figure 8 shows the predicted Doppler centroid for a LEO satellite using the following equation derived from [3]

$$f_D = -\frac{2}{\lambda}\{\omega_e R_s[\cos\theta_s \cos\alpha \sin\alpha_i + \sin\theta_s \cos\alpha_i] - \omega_s R_s \sin\gamma \sin\theta_s\},$$ (15)

where R_s is the satellite orbit's radius of curvature, ω_e and ω_s are the angular velocities of the earth and satellite respectively, θ_s is the squint angle (0 = side-looking), γ is the
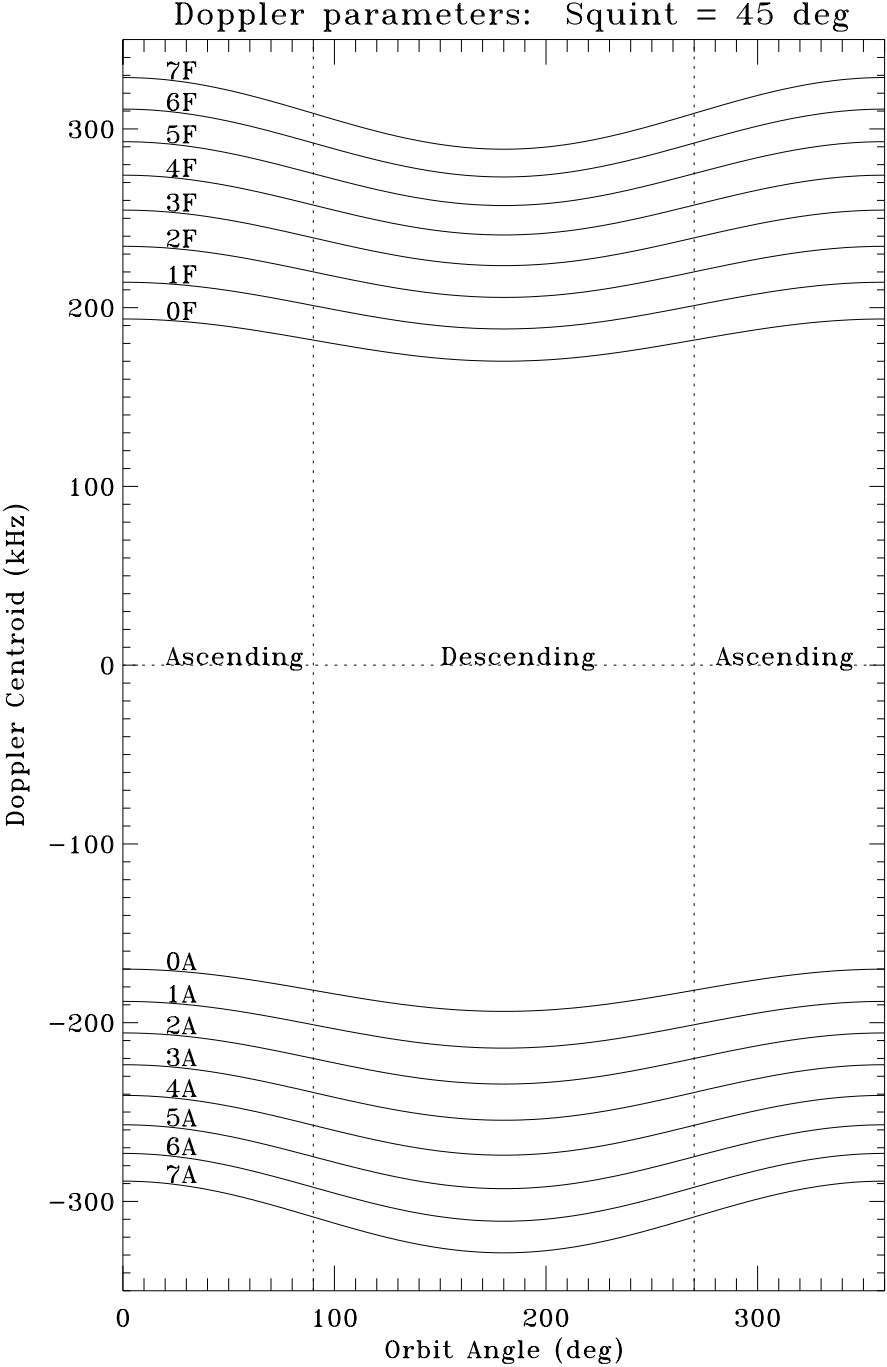
Figure 8: Doppler centroids vs. orbit angle, α, for a circular orbit with 108° inclination (SeaSAT's). Curves are labeled with identifiers for Subswath (1-8) and look (Fore/Aft).
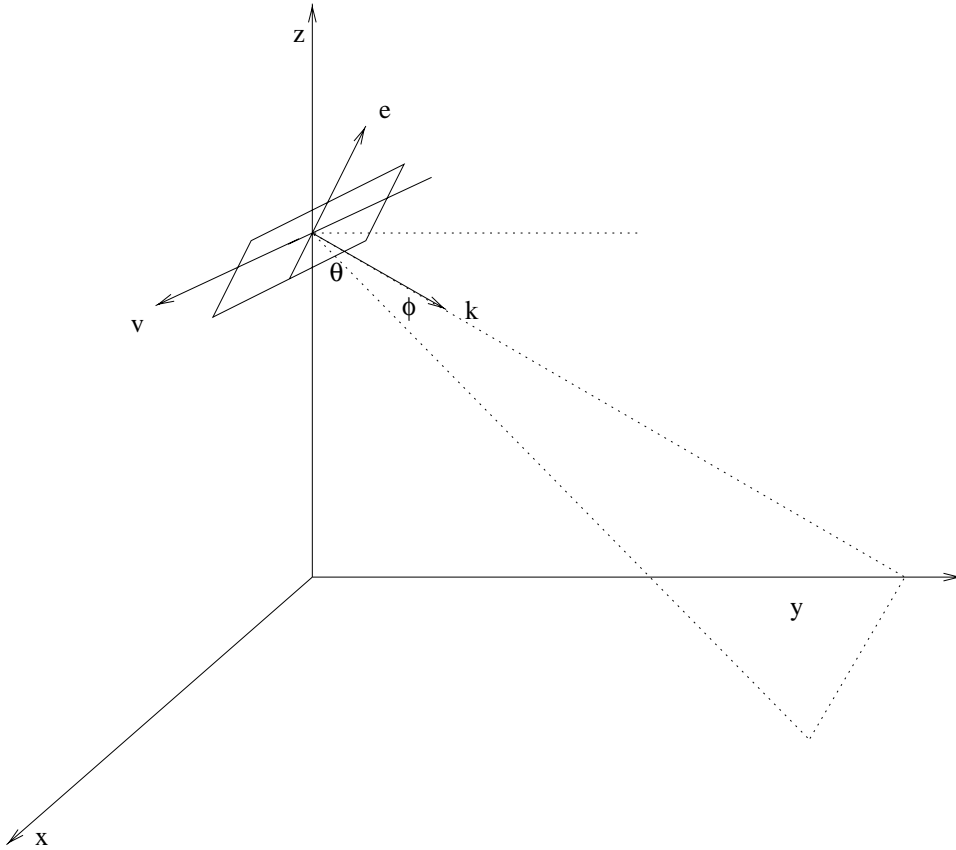
Figure 9: Squint geometry for a nominally "side-looking" antenna.

incidence angle, α_i is the inclination angle, and α is the orbital position angle (measured with respect to the equator in the plane of inclination). As written, this equation is specific to a right-looking satellite.

From the figure, we see fore and aft squints are separated by several hundred kilohertz. To extract the appropriate subswaths, the radar receiver must incorporate a tracking Doppler filter to follow the centroid for each swath. Note the beam configuration here is similar to that of the NSCAT and SASS sensors which also used Doppler filtering for range discrimination.

4.3.2 Effect on Polarization

Depending upon the choice of antenna architecture, the fore and aft squint of the sensor will have different polarization characteristics. One approach is to consider a nominally "side-looking" antenna that radiates fore- and aft-squinted beams (either simultaneous or switched). Another approach is to consider two physically different antennas oriented along the desired squint directions.

While the first approach is attractive, the combination of incidence angle and squint angle yields a polarization mixing such that the incident field on the ocean surface will consist of a combination of V and H polarizations (assuming a V-polarized transmitting antenna).

Consider an antenna at height h along the z-axis above the x-y plane oriented such that

the main beam of the antenna lies in the y-z plane (see Figure 9). The orientation of the propagation vector along boresight is

$$\hat{\mathbf{k}} = \hat{\mathbf{y}} \sin \theta - \hat{\mathbf{z}} \cos \theta, \tag{16}$$

and the orientation of the electric field is

$$\hat{\mathbf{e}} = \hat{\mathbf{y}} \cos \theta + \hat{\mathbf{z}} \sin \theta. \tag{17}$$

So as to use aperture efficiently, the antenna will be oriented somewhere near mid-swath. If the main beam is subsequently squinted forward or aft, then $\hat{\mathbf{k}}$ is rotated about the $\hat{\mathbf{e}}$-axis (note, not the z-axis) by the squint angle, ϕ ($\hat{\mathbf{e}}$ remains the same). The orientation of $\hat{\mathbf{e}}$ in the plane normal to the squinted $\hat{\mathbf{k}}$ now includes a horizontal component which varies as $\cos \theta \sin \phi$. Note that for small incidence angles and large squints, the polarization becomes more horizontal than vertical.

This polarization mixing effect may be undesirable because the scattering amplitude is best understood (i.e. model functions exist) for V (or H) polarization at Ku-band. Modeling efforts may be complicated if two polarizations must be considered.

The effect of the polarization mixing can be reduced by making the squint angles as small as is possible. It is not necessary to have orthogonal looks to obtain vector velocities. For example, ground based wind profilers regularly estimate horizontal winds using beams squinted only about 20° from zenith. Similarly HF current mapping radars usually have non-orthogonal looks. Required SNR for quality vector estimates will increase, however, if the angle between fore and aft looks becomes small. Also, orthogonal squint angles are desireable for wind-vector estimates from received power levels (scatterometry). This may not be critical to the sensor at hand if one plans to incorporate separate wind vector measurements.

Alternatively, one could design a squinted dual-beam or switched-beam antenna that maintains vertical polarization on each beam. However, this would likely be a fairly complicated antenna design. Given these issues, separate antennas for fore and aft looks, akin to a sensor like NSCAT or SASS, should be given consideration.

Polarization issues aside, the driving issue for the antenna architecture is obtaining sufficient dwell time to achieve the modest number of independent looks to reduce phase uncertainties. Given the antenna dimension parameters proposed for the current sensor that yield available looks on the order of 10, simultaneous beams are probably desirable.

4.4   MTF Effects

Surface Doppler velocity measurements include contributions from the phase velocities of Bragg-resonant waves and from the modulations of these waves by the longer gravity waves. Corrections for both effects are required to obtain surface current estimates. Proper correction for the Bragg-resonant waves requires some knowledge of their directional distribution, which is not well known at present. Moller et al. [26] have made measurements which support a simple model for directional spreading of Bragg-resonant capillary waves.

The effect of the Modulation Transfer Function (MTF) is to bias mean Doppler measurements because of the dependence of the backscattered power with the phase on the surface wave profile. Simply put, some parts of the wave produce more backscatter than others, so the mean reported Doppler shift is biased towards these portions of the wave. Graber et al. [27] employed a scattering model to include both Bragg and MTF effects in extracting current estimates from their interferometric measurements.

A substantial body of literature exists on field measurements of the MTF though little of the published literature directly addresses the impact of MTF on mean Doppler. Here we present a very simple analysis to predict the impact. The MTF is defined as the dimensionless measure of power fluctuation per unit wave slope of the long waves. It is commonly measured by correlating the power (AM) and Doppler (FM) channels of a scatterometer. The Doppler (radial) measurements are usually converted to the horizontal component of orbital velocity. We use the Ku-band measurements of Keller and Plant [28] obtained during the 1990 TOWARD experiment. In this study they measured MTFs at 45° incidence with magnitudes ranging from about 6 to 12, on average, and with phases of about 60° (leading the wave crests for advancing waves). There are fairly large measurement uncertainties in these values, but they are good enough for rough estimates. The MTF magnitude tends to be inversely related to wind speed: larger values at lower winds, smaller values at higher winds.

To estimate the influence of MTF on Doppler, we used the following procedure. A linear surface wave is prescribed with a height profile

$$z(x) = A\cos(\Omega t - Kx). \tag{18}$$

Without loss of generality, we can assume $t = 0$. The corresponding profiles of slope and orbital velocity (horizontal component) are given by

$$s(x) = KA\sin(Kx) \tag{19}$$
$$u(x) = -\Omega A\sin(Kx), \tag{20}$$

where A is the wave amplitude, K is the wavenumber, and Ω is the radian frequency $(= \sqrt{gK}$ for linear gravity waves). Assuming linear MTF theory, the backscattered power profile would look like

$$P(x) = \bar{P}[1 + mKA\sin(Kx + \phi)]. \tag{21}$$

where $\bar{P}$ is the mean power, m is the MTF magnitude, and ϕ is the MTF phase. The backscattered field magnitude, $E(x)$, is proportional to the square root of this expression.

Now, if we assume zero current, the average value of $u(x)$ is zero. A radar beam illuminating several cycles of this wave, however, would report a weighted mean velocity according to

$$\bar{u}_D = \left[\int E(x)\,dx\right]^{-1} \int u(x)E(x)\,dx \tag{22}$$

which is non-zero and represents the bias due to MTF.

For a very simple simulation, we assumed a monochromatic ocean wave of 100 m wavelength and various rms amplitudes. The table below shows rms amplitudes, rms slopes, and Doppler velocity biases for three values of MTF magnitude. The phase of the MTF is immaterial if we are illuminating several cycles of the wave.

The bolded numbers indicate the trend that would be expected in MTF with sea-state (which we assume is correlated with wind speed). From the table, biases for lower sea states are less than 5 cm/s and are approaching 20 cm/s for moderate seas. The bias shown for the largest amplitude waves is quite large, and is probably verging on the unrealistic, as rms slopes are also fairly large. These biases agree qualitatively with the X-band observations by Moller et al. [26] which were obtained at incidence angles greater than 60° for low to moderate seas.

Table 1: MTF-induced bias in Doppler velocity

σ_A (cm)	σ_s (deg)	u_D: m=6 (cm/s)	u_D: m=9 (cm/s)	u_D: m=12 (cm/s)
25	0.9	0.5	0.7	**0.9**
50	1.8	1.9	2.8	**3.9**
75	2.7	4.3	**6.6**	9.5
100	3.6	7.8	**13.**	21.
150	5.4	**19.**	36.	43.
200	7.2	**42.**	58.	64.

Real sea surfaces however, contain a spectrum of waves exhibiting group behavior that is not simulated here. Better quality estimates would come from a more realistic sea-surface profile than the simplistic cosine wave. This analysis should give some indication of the anticipated biases, however.

5   System Alternatives and Their Implications

The design and analysis performed here was preliminary only. We have not looked into hardware considerations for mass/cost estimates which may well influence the design direction. What we have done however, is to identify a viable system framework to work within. The benchmark design can be altered and refined within reason to meet the specific constraints and goals of a mission.

For the Ku-band single space-craft benchmark design a physical baseline of ≈ 21m was recommended. However examining Fig 7 reveals that even at a temporal spacing of 2ms (14m) the phase accuracy is still within our goals if the SNR is > 10dB. By iterating the design and refining some of the parameter choices a smaller baseline should be acheivable. An immediate option is, of course, to increase the transmit power.

The swathwidth of this system is smaller than that of satellite systems and this may be viewed as a shortcoming (the swathwidth of the current design is 360km on one side, while NSCAT's swathwidth was 600km). The swathwidth could be increased by increasing the number of ScanSAR positions. However the SNR of the subswaths will suffer because the dwell-time is further reduced. Furthermore, the ocean σ_0 rolls off fairly quickly with incidence angle further impacting additional subswaths. Again, an increase in transmit power will mitigate this.

Primarily we have focused on a single spacecraft system, and as such one of the key aims was to minimize the along-track baseline separation. Given this consideration, we chose a Ku-Band transmit frequency which has the additional, significant advantage of a wealth of scatterometer design and wind-retrieval algorithm development. In a dual space-craft configuration a longer physical baseline is probably more desirable, and will depend on whether the space-craft are tethered. If the space-craft are untethered and the goal is to maximize the separation L-band is an appropriate choice. The longer wavelength and ocean decorrelation time will enable a lengthened baseline. Furthermore, at longer wavelengths the orbit control and baseline knowledge requirements, while still stringent, are less exacting requirements than higher frequencies. One can effectively double the physical baseline by using a transmit fore (or aft), receive fore and aft simultaneously pulsing strategy. However if this approach is applied it is necessary to cohere the fore and aft radars.

6 Recommendations for Future Work

In order to test the system concept and identify outstanding measurement or technology application issues we recommend development and deployment of an airborne squint-mode along-track interferometric system. The key goals of such a program are:

1. to demonstrate the measurement technology by collecting highly squinted along-track interferometric data.

2. to characterize the directional dependence of interferometric measurements in order to establish an accurate construction of a surface velocity/current vector.

Ideally a prototype interferometer/scatterometer system similar to that outlined in this report would be constructed and flown. This was proposed to the 1998 Instrument Incubator Program (IIP) by one of the authors (SF). However, a second less expensive option is to adapt an airborne SAR to collect single-pass interferometric vector data as a "proof of concept". In particular JPL's AIRSAR is a convenient platform for such an experiment. The AIRSAR system currently collects only radial velocities in a single-pass thereby requiring a successive overlapping pass to infer a surface current vector. We propose an adaptation to the L-band system (the most appropriate from power considerations) that will enable vector measurements in a single-pass by utilizing simultaneous fore and aft beams. This can be acheived through insertion of a relatively simple phase-shifter network before the antenna feed. Although the radiometric calibration of AIRSAR is not as accurate as one would like for scatterometry, this is still a viable platform for demonstrating the system principle in an economic manner.

6.1 Airborne Deployments

Airborne deployments of the SAR interferometer/scatterometer testbed are proposed over Monterey Bay and Santa Barbara. These sites have extensive in situ instrumentation and are continuously monitored by HF current mapping radars. As such these experiments will provide ideal data sets from which to develop a precise method for estimating the surface current from interferometric measurements. Collaboration with the PI's at these site will provide a unique opportunity for validation of the measurements

6.2 Data Characterization

The primary goal of the proposed airborne program is to demonstrate the ability of this technology to create unambigous wind-vector/surface velocity map. Toward this end we anticipate that incorporating the velocity measurements into scatterometric wind-retrieval algorithms will be fairly straightforward. However, resolving a surface velocity vector is less straightforward, to a large degree due to the lack of comparative data available to date. Data collected in these experiments will help address this general shortfall. To generate a relationship between the physical ocean processes and the measurement need to be characterized in a tractable manner. This will likely take the form of model functions that enable translation of the individual radial velocity measurements to a radial surface current and subsequently to a surface current vectors. The goal here is to find a starting point for these model functions, both to correct for the Bragg phase-speed and for MTF biases. MTF biases are a function of a number of factors including angle with respect to the

wind, sea-state and measurement resolution. We will study the effects of resolution scales on MTF biases by selective area averaging.

The model functions will rely on the wind-speed and direction measurements which can be inferred from the scatterometry process. The model development will be initial in that it will be limited by the range of conditions over which the input data was gathered. As more data is collected the models can be refined in a similar process by which scatterometery model-functions have developed over the years.

7 Conclusions

This study evaluated the feasibility of a spaceborne scatterometer/along-track interferometer for the measurement of coincident wind and surface velocity vectors at the ocean surface. Such a system provides a solution to the ambiguity problem in scatterometry through the introduction of an additional measurement in the wind retrieval process: the Doppler velocity. In addition to the direct value to scatterometry, the production of coincident wind and velocity vector maps can provide data on the ocean surface wind stress, a parameter identified as a key missing variable for air-sea interaction and climate modelling research.

A benchmark system design and performance prediction was presented for a Ku-band single space-craft configuration. We found that the performance predictions of the benchmark design met our measurement goals. However, this design is extremely preliminary, with the intention being to prove feasibility and develop the fundamental system concept. Depending on platform constraints and possibly refined measurement requirements there is a great deal of flexibility within the initial framework presented here.

The nominal design consists of two sets of four beams separated by an along-track baseline. Each set of four consists of highly squinted fore and aft beams looking from both sides of the space-craft. Such a design enables backscatter and radial velocity measurements from different azimuth directions for surface velocity and wind vector retrieval.

To gain swathwidth, we propose an unfocused ScanSAR design with 8 subswaths. The ScanSAR configuration does not degrade the measurement resolution because the ocean decorrelation is the limiting factor in this design. However, scanning in elevation does decrease the dwell time and therefore the number of looks for each resolution cell. The current design has a swathwidth of over 350km on one-side.

The highly squinted geometry of the fore and aft beams impart a large Doppler shift on the returns, which varies as a function of the orbit position and the ScanSAR position. This necessitates using tracking Doppler filters to follow the centroid of each swath. This implementation is similar to the designs of NSCAT and SASS.

In summary, this preliminary study found that a spaceborne scatterometer/interferometer is certainly feasible within the measurement goals set forth here. To further develop this concept we recommend airborne test-bed deployments over well characterized regions. In particular an economic option for a "proof of concept" AIRSAR campaign was identified. More detailed plans of the hardware modifications, experiments and data characterization are available upon request.

References

[1] L.C. Schroeder, D.H. Boggs, G. Done, I.M. Halberstam, W.L. Jones, W.J. Pierson, and F.J. Wentz, "The relationship between wind vector and normalized radar cross section used to derive SEASAT-A satellite scatterometer winds", *Journal of Geophysical Research*, vol. 87, no. C5, pp. 3318–3336, 1982.

[2] M. A. Donelan and Jr. W. J. Pierson, "Radar scattering and equilibrium ranges in wind-generated waves with application to scatterometry", *Journal of Geophysical Research*, vol. 92, no. C5, pp. 4971–5029, 1987.

[3] A. Stoffelan, "Toward the true near surface wind speed: Error modelling and calibration using triple collocation", *Journal of Geophysical Research*, vol. 103, no. c4, pp. 7755–7766, 1998.

[4] S. J. Shaffer, R. S. Dunbar, S. V. Hsiao, and D. G. Long, "A median-filter-based ambiguity removal algorithm for NSCAT", *IEEE Transaction on Geoscience and Remote Sensing*, vol. 29, no. 1, pp. 167–174, 1991.

[5] D. G. Long and J. M. Mendel, "Identifiability in wind estimation from scatterometer measurements", *IEEE Transaction on Geoscience and Remote Sensing*, vol. 29, no. 2, pp. 268–276, 1991.

[6] M. G. Wurtele, P. M. Woiceshyn, S. Pereherych, M. Borowsky, and W. S. Appleby, "Wind direction alias removal studies of Seasat scatterometer-derived wind fields", *Journal of Geophysical Research*, vol. 87, no. C5, pp. 3365–3377, 1982.

[7] R. M. Goldstein, T. P. Barnett, and H. A. Zebker, "Remote sensing of ocean currents", *Science*, vol. 246, pp. 1282–1285, 1989.

[8] C. C. Wackerman, C. L. Rufenack, R. A. Schuchman, J. A. Johannessen, and K. L. Davidson, "Wind vector retrieval using ERS-1 synthetic aperture radar imagery", *IEEE Transaction on Geoscience and Remote Sensing*, vol. 36, no. 6, pp. 1343–1352, 1996.

[9] P. W. Vachon and F. W. Dobson, "Validation of wind vector retrieval from ERS-1 SAR images over the ocean", *The Global Atmosphere and Ocean System*, vol. 5, pp. 177–187, 1996.

[10] S. Lehner, J. Horstmann, W. Koch, and W. Rosenthal, "Mesoscale wind measurements using recalibration ERS SAR images", *Journal of Geophysical Research*, vol. 103, no. C4, pp. 7847–7856, 1998.

[11] K. K. Kahma and M. A. Donelan, "A laboratory study of the minimum wind speed for wind wave generation", *Journal of Fluid Mechanics*, vol. 192, pp. 339–364, 1987.

[12] G. Caulliez, N. Ricci, and R. Dupont, "The generation of the first visible wind waves", *Physics of Fluids*, vol. 10(4), pp. 757–759, 1998.

[13] W.J. Plant, "Bragg scattering of electromagnetic waves from the air/sea interface", in *Surface Waves and Fluxes*, G. L. Geernaert and W. J. Plant, Eds., vol. 2, chapter 11, pp. 41–108. Kluwer Academic Publishers, 1990.

[14] W.L. Bragg, "The diffraction of of short electromagnetic waves by a crystal", *Proc. Cambridge Phil. Soc.*, vol. 17, pp. 43, 1913.

[15] R.K. Moore and A.K. Fung, "Radar determination of winds at sea", *Proceedings of the IEEE*, vol. 67, no. 11, pp. 1504–1520, 1979.

[16] K.S. Miller and M.M. Rochwarger, "A covariance approach to spectral moment estimation", *IEEE Transactions on Information Theory*, vol. 18, no. 5, pp. 588–596, 1972.

[17] B. Kinsman, *Wind Waves*, Prentice-Hall, Inc., 1965.

[18] W.C. Keller and J.W. Wright, "Microwave scattering and the straining of wind-generated waves", *Radio Science*, vol. 10, pp. 139–147, 1975.

[19] J.W. Wright, W.J. Plant, W.C. Keller, and W.L. Jones, "Ocean wave–radar modulation transfer functions from the west coast experiment", *Journal of Geophysical Research*, vol. 85, no. C9, pp. 4957–4966, 1980.

[20] W.J. Plant, "The modulation transfer function: Concept and applications", in *Radar Scattering From Modulated Wind Waves*, J. Komen and W.A. Oost, Eds., pp. 155–172. Kluwer Academic Publishers, 1989.

[21] W.J. Plant, E.A. Terray, R.A. Pettit Jr., and W.C. Keller, "The dependence of microwave backscatter from the sea on illuminated area, correlation times and lengths", *Journal of Geophysical Research*, vol. 99, no. C5, pp. 9705–9723, 1994.

[22] R.E. Carande, "Estimating ocean coherence time using dual-baseline interferometric synthetic aperture radar", *IEEE Transaction on Geoscience and Remote Sensing*, vol. 32, no. 4, pp. 846–854, 1994.

[23] D. Middleton, *An Introduction to Statistical Communication Theory*, McGraw-Hill, New York, 1960.

[24] R.D. Chapman, B.L. Gotwols, and R.E. Sterner II, "On the statistics of the phase of microwave backscatter from the ocean surface", *Journal of Geophysical Research*, vol. C8, pp. 16923–16301, 1994.

[25] R.K. Raney, "SAR response to partially coherent phenomena", *IEEE Transaction on Antennas and Propagation*, vol. AP-28, pp. 777–787, 1980.

[26] D. Moller, S.J. Frasier, D.L. Porter, and R.E. McIntosh, "Radar-derived interferometric surface currents and their relationship to subsurface current structure", *Journal of Geophysical Research*, vol. 103, no. C6, pp. 12839–12852, 1998.

[27] H.C. Graber, D.R. Thompson, and R.E. Carande, "Ocean surface features and currents measured with synthetic aperture radar interferometry and HF radar", *Journal of Geophysical Research*, vol. 101, no. C11, pp. 25813–25832, 1996.

[28] W.C. Keller and W.J. Plant, "Cross sections and modulation transfer functions at L and Ku bands measured during the tower ocean wave and radar dependence experiment", *Journal of Geophysical Research*, vol. 95, no. C9, pp. 16277–16289, 1990.

Appendix A: Design Example - Subswath 3

The table below lists the parameters used to generate a performance analysis, and their values for subswath 3.

Fact Sheet: Subswath 3

Altitude	770 km	Antenna Length	7 m
Velocity	7470.01 m/s	Antenna Width	.5 m
Frequency	13.8 GHz	Antenna Elements (width)	
Bandwidth	1 MHz	Mechanical Boresight	26.2614 deg
Transmit Peak Power	15 W	Electrical Steering	
Pulse Duration	50 micro-s	Noise Temperature	800 K
Proc. Doppler Bandwidth	100 Hz	System Losses	-4.5 dB
Data Rate	4.0076 Mbps	ISLR	-15 dB
Bits per Sample	4	Oversampling factor	1.2
Data Window Start	163.018 micro-s	Radius of Curvature	6378 km
Near Range Look	25 deg	PRF	2.15 kHz

Boresight Parameters			
Look Angle	26.2614 deg	Brightness	-8.6283 dB
SNR	22.521 dB	Noise-Equiv. σ_0	-30.9487 dB
Signal Level	-130.372 dB	Range Ambig	-35.7953 dB
Thermal Noise Level	-152.893 dB	Az Ambig	-34.382 dB
Range Resolution (ground)	261.774 m	Slant Range	871.638 km
Azimuth Resolution (4-look)	298.8 m	Incidence Angle	29.7281 deg

Data Swath	Start	End
Look Angle	25 deg	27.4894 deg
Delay	163.018 micro-s	357.258 micro-s
Location	364.099 km	407.712 km
Range Ambiguity Level	-28.6381 dB	-24.5836 dB
Noise-Equivalent σ_0	-23.1852 dB	-22.9814 dB

Swath Width	43.613 km	Beam-Limited Swath	
Wavelength	2.17241 cm	Radiated Power	1.6125 W
El. Beamwidth	2.25 deg	Pulses in Air	13
Az. Beamwidth	0.15 deg	Data Window	194.24 micro-s
Directivity	49.7345 dB	IPP	465.116 micro-s

Signal

The signal strength is given by:

$$S = \left(\frac{1}{4\pi}\right)^3 P G_t G_r \frac{\lambda^2}{r^4}(r\theta_{\text{az}})\frac{C}{2\sin\theta_l B_r}(\tau_d B_r)\sigma(\theta_i)\eta_{\text{prop}}\eta_{\text{sys}} \tag{23}$$

where, presently, $G_t = G_r \equiv G$, P is the "Power" parameter from Common Parameters Table; r is the range at look angle θ_l, corresponding to incidence angle θ_i, at which the brightness is $\sigma_0(\theta_i)$. λ is the wavelength (all units are MKS), B_r is the range bandwidth, B_c is the oversampled complex bandwidth: $B_c = 1.2B_r$. τ_d is the pulse duration, and the η's are the loss terms for both propagation and system losses. Table 2 enumerates these quantities at the boresight (26.2614 deg).

Radar Equation Term	Value
λ	2.17241 cm
P	15 W
G	49.7345 dB
r	871.638 km
θ_{az}	0.15 deg
θ_l	26.2614 deg
θ_i	29.7281 deg
$\sigma(\theta_i)$	-8.6283 dB
B_r	1 MHz
B_c	1.2 MHz
τ_d	50 micro-s
η_{prop}	0 dB
η_{sys}	-4.5 dB
Signal Level	-130.372 dB

Table 2: Contributions to the signal level at boresight (26.2614 deg). See text and (23).

Radar Equation Term	Contribution
λ	-33.2612 dB
$(4\pi)^{-3}$	-32.9763 dB
t_P	11.7609 dB
$G_t G_r$	99.469 dB
r^{-4}	-237.613 dB
Azimuth Dimension	33.583 dB
Cross-Track Dimension	24.8041 dB
Pulse Compression	16.9897 dB
σ_0	-8.6283 dB
Propagation Losses	0 dB
System Losses	-4.5 dB
Signal Level	-130.372 dB

Table 3: Signal Strength contributions from the radar equation at the boresight (26.2614 deg) for this system (ysc25).

SNR Performance

The brightness model used for this analysis is from Ulaby.Moore and Fung: Microwave Remote Sensing Vol 2. We use his results for the radar backscattering from ocean for the range ambiguity analysis, and the results from ocean are used for all other analyses. Given this model, the SNR of this system should be better than 10.3667 dB everywhere. The thermal noise is down by at least -13.6116 dB, the range and azimuth ambiguities by -24.5835 dB and -34.382 dB, respectively. The Noise-Equivalent σ_0 (i.e., the scattering brightness, σ_0, at which the SNR becomes 1) is better than -22.9814 dB everywhere across the swath, and at the best location is -30.9465 dB. Figure 10 shows this quantity as a function of the swath, and 11 shows the signal and noise levels across the swath. The radar equation terms contributing to the SNR at the boresight (26.2614 deg) are given in Table 4.

Radar Equation Term	Contribution
λ	-33.2612 dB
$(4\pi)^{-3}$	-32.9763 dB
t_P	11.7609 dB
$G_t G_t$	99.469 dB
r^{-4}	-237.613 dB
Azimuth Dimension	33.583 dB
Cross-Track Dimension	24.8041 dB
Pulse Compression	16.9897 dB
σ_0	-8.6283 dB
Propagation Losses	0 dB
System Losses	-4.5 dB
Thermal Noise	152.893 dB
Other Noise	-9.57512 dB
SNR	12.9459 dB

Table 4: SNR contributions from the radar equation at the boresight (26.2614 deg) for this subswath.

Gain Patterns

The directivity of this configuration is computed to be 49.7345 dB. Presently no taper is assumed in elevation or azimuth, nor have we looked at the effects of squinted geometries on the beam patterns (this is one issue that UMass will investigate). The range beamwidth is 2.25 deg and the azimuth beamwidth, 0.15 deg. The gain patterns for this antenna are plotted in Figures 12–13.

Pulse Timing and Geometry

The pulse timing diagram is displayed (to scale) in Figure 14. There are 13 pulses in
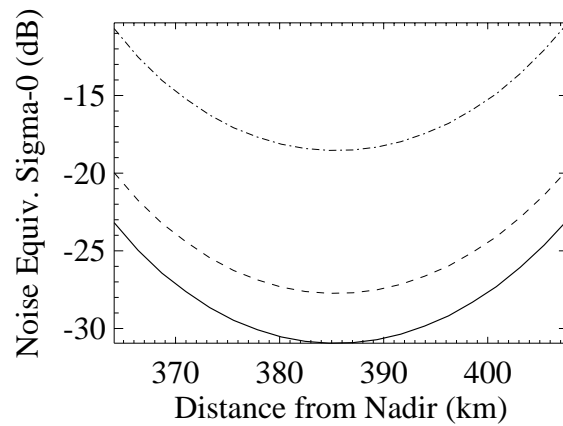
Figure 10: Noise-Equivalent σ_0 plotted as a function of distance along the subswaths. The thick line is for SNR = 0 dB; the dashed line is for SNR =3 dB and the dash-dot line for 10 dB.
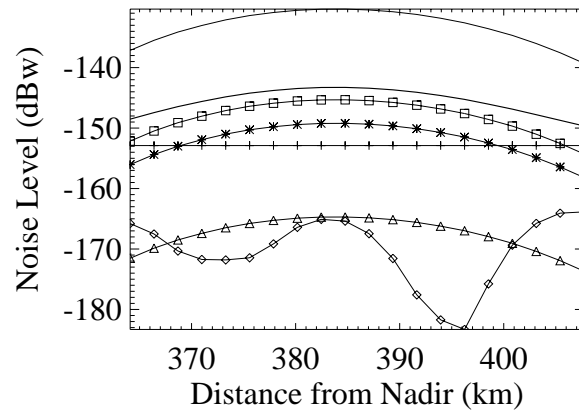
Figure 11: Components of the noise level compared to the signal level for each subswath in this system. Plotted are: signal level (thin line), total noise (thick line), thermal noise (crosses), quantization noise (asterisks), range ambiguity level (diamonds), azimuth ambiguity side-lobe ratio (AASR) (triangles) and integrated side-lobe ratio (ISLR) (squares).
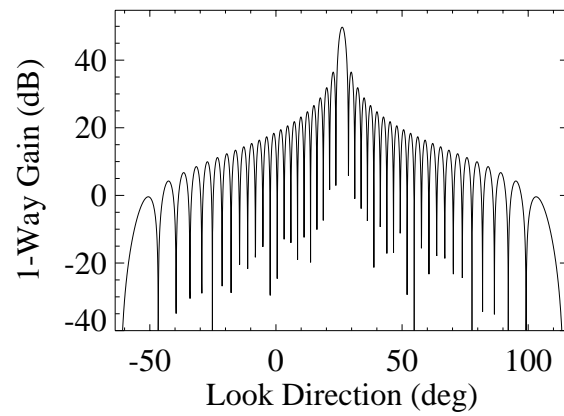
Figure 12: Antenna elevation gain pattern (composite of transmit and receive).
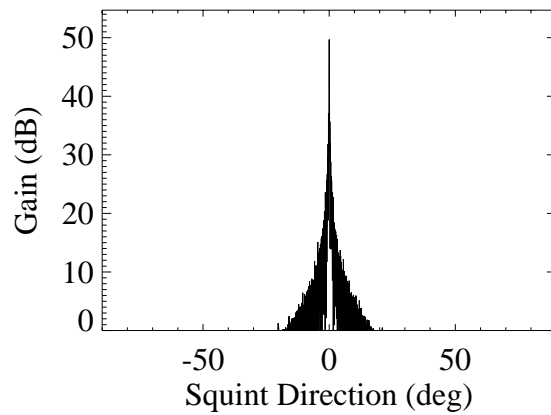
Figure 13: Antenna azimuth gain pattern (composite of transmit and receive).

the air at any one time with this pulse timing scheme.
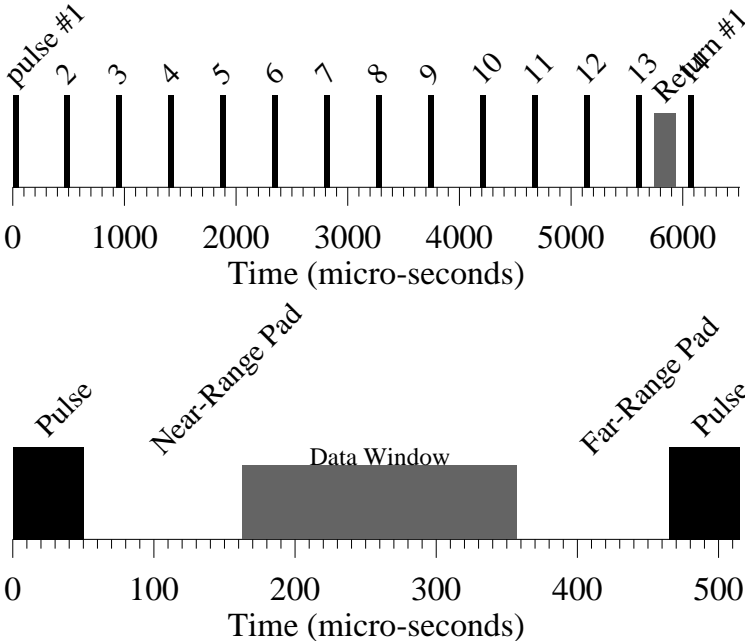
Figure 14: Pulse timing diagram.

Appendix B: Performance Fact Sheets

Subswath 1

Version	ysc20	Date	November 2, 1998
Bandwidth	1 MHz	Mechanical Boresight	21.4577 deg
Data Window Start	161.902 micro-s		
Near Range Look	20.2 deg	PRF	2.24 kHz
Boresight Parameters			
Look Angle	21.4577 deg	Brightness	-4.89348 dB
SNR	27.8163 dB	Noise-Equiv. σ_0	-32.5104 dB
Signal Level	-125.255 dB	Range Ambig	-55.9643 dB
Thermal Noise Level	-153.072 dB	Az Ambig	-34.7272 dB
Range Resolution (ground)	316.626 m	Slant Range	835.213 km
Azimuth Resolution (4-look)	298.8 m	Incidence Angle	24.2035 deg
Data Swath		Start	End
Look Angle		20.2 deg	22.6895 deg
Delay		161.902 micro-s	320.702 micro-s
Location		285.756 km	325.546 km
Range Ambiguity Level		-57.2949 dB	-29.9905 dB
Noise-Equivalent σ_0		-24.8252 dB	-24.5013 dB
Swath Width	39.79 km	Beam-Limited Swath	
Wavelength	2.17241 cm	Radiated Power	1.68 W
El. Beamwidth	2.25 deg	Pulses in Air	13
Az. Beamwidth	0.15 deg	Data Window	158.8 micro-s
Directivity	49.7345 dB	IPP	446.429 micro-s

Subswath2

Version	ysc23	Date	November 2, 1998
Bandwidth	1 MHz	Mechanical Boresight	23.8595 deg
Data Rate	3.7136 Mbps	ISLR	-15 dB
Data Window Start	169.11 micro-s		
Near Range Look	22.6 deg	PRF	2.2 kHz
Boresight Parameters			
Look Angle	23.8595 deg	Brightness	-6.75976 dB
SNR	25.1738 dB	Noise-Equiv. σ_0	-31.7331 dB
Signal Level	-127.82 dB	Range Ambig	-36.261 dB
Thermal Noise Level	-152.993 dB	Az Ambig	-34.7764 dB
Range Resolution (ground)	286.348 m	Slant Range	852.145 km
Azimuth Resolution (4-look)	298.8 m	Incidence Angle	26.9575 deg
Data Swath		Start	End
Look Angle		22.6 deg	25.0894 deg
Delay		169.11 micro-s	344.71 micro-s
Location		324.086 km	365.626 km
Range Ambiguity Level		-34.2964 dB	-31.9264 dB
Noise-Equivalent σ_0		-24.0072 dB	-23.7558 dB
Swath Width	41.54 km	Beam-Limited Swath	
Wavelength	2.17241 cm	Radiated Power	1.65 W
El. Beamwidth	2.25 deg	Pulses in Air	13
Az. Beamwidth	0.15 deg	Data Window	175.6 micro-s
Directivity	49.7345 dB	IPP	454.545 micro-s

Subswath 3

Version	ysc25	Date	November 2, 1998
Bandwidth	1 MHz	Mechanical Boresight	26.2614 deg
Data Rate	4.0076 Mbps	ISLR	-15 dB
Data Window Start	163.018 micro-s	Radius of Curvature	6378 km
Near Range Look	25 deg	PRF	2.15 kHz
Boresight Parameters			
Look Angle	26.2614 deg	Brightness	-8.6283 dB
SNR	22.521 dB	Noise-Equiv. σ_0	-30.9487 dB
Signal Level	-130.372 dB	Range Ambig	-35.7953 dB
Thermal Noise Level	-152.893 dB	Az Ambig	-34.382 dB
Range Resolution (ground)	261.774 m	Slant Range	871.638 km
Azimuth Resolution (4-look)	298.8 m	Incidence Angle	29.7281 deg
Data Swath		Start	End
Look Angle		25 deg	27.4894 deg
Delay		163.018 micro-s	357.258 micro-s
Location		364.099 km	407.712 km
Range Ambiguity Level		-28.6381 dB	-24.5836 dB
Noise-Equivalent σ_0		-23.1852 dB	-22.9814 dB
Swath Width	43.613 km	Beam-Limited Swath	
Wavelength	2.17241 cm	Radiated Power	1.6125 W
El. Beamwidth	2.25 deg	Pulses in Air	13
Az. Beamwidth	0.15 deg	Data Window	194.24 micro-s
Directivity	49.7345 dB	IPP	465.116 micro-s

Subswath 4

Version	ysc274	Date	November 2, 1998
Bandwidth	1 MHz	Mechanical Boresight	28.7334 deg
Data Rate	4.3512 Mbps	ISLR	-15 dB
Data Window Start	173.17 micro-s	Radius of Curvature	6378 km
Near Range Look	27.47 deg	PRF	2.1 kHz

Boresight Parameters			
Look Angle	28.7334 deg	Brightness	-10.5557 dB
SNR	19.7912 dB	Noise-Equiv. σ_0	-30.1459 dB
Signal Level	-133 dB	Range Ambig	-35.6114 dB
Thermal Noise Level	-152.791 dB	Az Ambig	-33.7012 dB
Range Resolution (ground)	240.937 m	Slant Range	894.685 km
Azimuth Resolution (4-look)	298.8 m	Incidence Angle	32.6001 deg

Data Swath		Start	End
Look Angle		27.47 deg	29.9594 deg
Delay		173.17 micro-s	388.97 micro-s
Location		407.362 km	453.504 km
Range Ambiguity Level		-29.0022 dB	-36.7244 dB
Noise-Equivalent σ_0		-22.3558 dB	-22.213 dB

Swath Width	46.142 km	Beam-Limited Swath	
Wavelength	2.17241 cm	Radiated Power	1.575 W
El. Beamwidth	2.25 deg	Pulses in Air	13
Az. Beamwidth	0.15 deg	Data Window	215.8 micro-s
Directivity	49.7345 dB	IPP	476.19 micro-s

Subswath 5

Version	ysc299	Date	November 2, 1998
Bandwidth	1 MHz	Mechanical Boresight	31.1656 deg
Data Rate	5.0688 Mbps	ISLR	-15 dB
Data Window Start	139.935 micro-s	Radius of Curvature	6378 km
Near Range Look	29.9 deg	PRF	2.2 kHz

Boresight Parameters			
Look Angle	31.1656 deg	Brightness	-12.4586 dB
SNR	17.3967 dB	Noise-Equiv. σ_0	-29.6558 dB
Signal Level	-135.597 dB	Range Ambig	-45.9342 dB
Thermal Noise Level	-152.993 dB	Az Ambig	-34.7764 dB
Range Resolution (ground)	223.814 m	Slant Range	920.703 km
Azimuth Resolution (4-look)	298.8 m	Incidence Angle	35.4499 deg

Data Swath		Start	End
Look Angle		29.9 deg	32.3894 deg
Delay		139.935 micro-s	379.875 micro-s
Location		452.369 km	501.472 km
Range Ambiguity Level		-21.768 dB	-25.5386 dB
Noise-Equivalent σ_0		-21.8156 dB	-21.728 dB

Swath Width	49.103 km	Beam-Limited Swath	
Wavelength	2.17241 cm	Radiated Power	1.65 W
El. Beamwidth	2.25 deg	Pulses in Air	14
Az. Beamwidth	0.15 deg	Data Window	239.94 micro-s
Directivity	49.7345 dB	IPP	454.545 micro-s

Subswath 6

Version	ysc323	Date	November 2, 1998
Bandwidth	1 MHz	Mechanical Boresight	33.5681 deg
Data Rate	5.87045 Mbps	ISLR	-15 dB
Data Window Start	107.44 micro-s	Radius of Curvature	6378 km
Near Range Look	32.3 deg	PRF	2.286 kHz

Boresight Parameters			
Look Angle	33.5681 deg	Brightness	-14.3476 dB
SNR	14.9769 dB	Noise-Equiv. σ_0	-29.121 dB
Signal Level	-138.183 dB	Range Ambig	-30.6125 dB
Thermal Noise Level	-153.16 dB	Az Ambig	-34.304 dB
Range Resolution (ground)	209.478 m	Slant Range	950.127 km
Azimuth Resolution (4-look)	298.8 m	Incidence Angle	38.2929 deg

Data Swath		Start	End
Look Angle		32.3 deg	34.7894 deg
Delay		107.44 micro-s	374.79 micro-s
Location		499.65 km	552.241 km
Range Ambiguity Level		-23.1112 dB	-19.3421 dB
Noise-Equivalent σ_0		-21.2707 dB	-21.1738 dB

Swath Width	52.591 km	Beam-Limited Swath	
Wavelength	2.17241 cm	Radiated Power	1.7145 W
El. Beamwidth	2.25 deg	Pulses in Air	15
Az. Beamwidth	0.15 deg	Data Window	267.35 micro-s
Directivity	49.7345 dB	IPP	437.445 micro-s

Subswath 7

Version	ysc347	Date	November 2, 1998
Bandwidth	1 MHz	Mechanical Boresight	35.9708 deg
Data Rate	6.3184 Mbps	ISLR	-15 dB
Data Window Start	77.05 micro-s	Radius of Curvature	6378 km
Near Range Look	34.7 deg	PRF	2.2 kHz

Boresight Parameters			
Look Angle	35.9708 deg	Brightness	-16.2492 dB
SNR	12.1921 dB	Noise-Equiv. σ_0	-28.2389 dB
Signal Level	-140.801 dB	Range Ambig	-31.6723 dB
Thermal Noise Level	-152.993 dB	Az Ambig	-34.7764 dB
Range Resolution (ground)	197.194 m	Slant Range	983.834 km
Azimuth Resolution (4-look)	298.8 m	Incidence Angle	41.1692 deg

Data Swath		Start	End
Look Angle		34.7 deg	37.1894 deg
Delay		77.05 micro-s	376.3 micro-s
Location		550.283 km	607.057 km
Range Ambiguity Level		-25.8396 dB	-14.258 dB
Noise-Equivalent σ_0		-20.3802 dB	-20.186 dB

Swath Width	56.774 km	Beam-Limited Swath	
Wavelength	2.17241 cm	Radiated Power	1.65 W
El. Beamwidth	2.25 deg	Pulses in Air	15
Az. Beamwidth	0.15 deg	Data Window	299.25 micro-s
Directivity	49.7345 dB	IPP	454.545 micro-s

Subswath 8

Version	ysc371	Date	November 2, 1998
Bandwidth	1 MHz	Mechanical Boresight	38.3738 deg
Data Rate	7.33664 Mbps	ISLR	-15 dB
Data Window Start	72.415 micro-s	Radius of Curvature	6378 km
Near Range Look	37.1 deg	PRF	2.27 kHz
Boresight Parameters			
Look Angle	38.3738 deg	Brightness	-18.1678 dB
SNR	9.66607 dB	Noise-Equiv. σ_0	-27.6252 dB
Signal Level	-143.463 dB	Range Ambig	-26.9332 dB
Thermal Noise Level	-153.129 dB	Az Ambig	-34.5234 dB
Range Resolution (ground)	186.579 m	Slant Range	1022.57 km
Azimuth Resolution (4-look)	298.8 m	Incidence Angle	44.0858 deg
Data Swath		Start	End
Look Angle		37.1 deg	39.5894 deg
Delay		72.415 micro-s	409.335 micro-s
Location		604.933 km	666.769 km
Range Ambiguity Level		-23.2418 dB	-23.94 dB
Noise-Equivalent σ_0		-19.7467 dB	-19.7518 dB
Swath Width	61.836 km	Beam-Limited Swath	
Wavelength	2.17241 cm	Radiated Power	1.7025 W
El. Beamwidth	2.25 deg	Pulses in Air	16
Az. Beamwidth	0.15 deg	Data Window	336.92 micro-s
Directivity	49.7345 dB	IPP	440.529 micro-s

Appendix C: Definitions and Equations

Parameter Descriptions

Timing Parameters

"Altitude" is the height of the radar platform above the planetary ellipsoid. This ellipsoid is determined by the local "Radius of Curvature". "PRF" is the single-channel pulse-repetition frequency. The "Swath Width" refers to the digitized swath. The "Near-Range Look Angle" is the look angle (not incidence angle) the the beginning of the swath. The "Min. Near-Range Pad" and "Min. Far-Range Pad" refer to the minimum time required between the end of the transmitted pulse and the beginning of the data window, and the end of the data window and the beginning of the next transmit pulse, respectively. (See the section on Geometry and Pulse Timing for more detailed discussion of these parameters.)

System Parameters

"Frequency" is the center or carrier frequency, "Bandwidth" is the complex range-bandwidth of the transmitted chirp. The "Frequency" parameter subsumes any frequency offset for the bandwidth. Thus, the transmitted frequencies should be from $\text{Frequency} - \text{Bandwidth}/2$ to $\text{Frequency} + \text{Bandwidth}/2$. The "Power" is total peak power radiated out of the antenna, after any system losses in the antenna feed and T/R module inefficiency. This is part of the model and needs to be better defined. The "Noise Temperature" needs to be defined. So do the "System Losses", a negative number. The "Quant. Bits" parameter is the number of bits used to quantize each real sample. Finally, the "Bandwidth Oversampling" is multiplied by the "Bandwidth" to obtain the complex Bandwidth, the latter of which is one-half the digitization rate.

Other Parameters

The "Doppler Bandwidth" is the bandwidth to which the azimuth data will be processed, usually just less than the PRF. The "Backscatter Model" refers to the type of scene used to obtain the brightness, and refers to the models of Ulaby. (See the section on SNR and brightness models.) "Polarization" is self-explanatory, and the "Radius of Curvature" refers to the local radius of curvature used for geometric calculations, and would vary with latitude.

Data Rate

The "Data Rate" is determined by:

$$2 \times \text{Bits per Sample} \times \text{PRF} \times \text{nRangeSamples} \tag{24}$$

where the number of range samples is given by:

$$\text{nint}(\text{Complex Bandwidth} \times \text{Oversampling} \times \text{Data Window}) \tag{25}$$

Resolution

The resolution on the ground (in the range direction) is given by:

$$\delta r = 0.866 \frac{C}{2 B_r \sin \theta_i} \tag{26}$$

where C is the speed of light, B_r is the range bandwidth and $theta_i$ is the angle of incidence (at the ground). See the Geometry section for the calculation of θ_i.

Performance

SNR-Equivalent σ_0

To characterize the performance of this system, we have computed the SNR-equivalent σ_0 for particular values of Signal-to-Noise Ratio (SNR). This quantity is defined as the value of the scattering cross-section, σ_{SNR}, where the SNR achieves a particular value, and is computed from:

$$\sigma_{\mathrm{SNR}} = \sigma_0 \frac{T/S}{\mathrm{SNR}^{-1} - f}, \tag{27}$$

where σ_0 is the scattering cross section used to compute the signal and noise levels, S is the signal level, T is the thermal noise, and $N = fS$ is the contribution to the total noise from all sources other than thermal noise (these are proportional to the signal). See Tables 2 and 3 for details on each of these components.

Thermal Noise

The thermal noise bandwidth is estimated from the noise temperature. This model needs improvement:

$$N_T = kTB_c \tag{28}$$

where k is the Boltzmann constant.

Range Ambiguities

One must assume a brightness model for the backscatter as a function of incidence angle in order to compute the range ambiguities. For this calculation, the model used is ocean (see the section on Performance, brightness subsection). Given this model, and an antenna gain pattern as a function of look angle (see Antenna section) we compute the range ambiguity:

$$\mathrm{RA} = S^-(0) + \sum_i S^-(i) + S^+(i), \quad i = 1, \ldots; \quad t(i) > t_h \tag{29}$$

where $S(i)$ is the signal level (in watts) received at the antenna (23) at time $t(i) = t_0 - i/\mathrm{PRF}$ and t_0 is the round trip time for the point at which we are computing the range ambiguity. ($t_h = 2C/h$, where h is the radar platform altitude.) Note that for $i \neq 0$ we must sum over the signal contributed from both the θ_l and the $-\theta_l$ look directions, symbolized here by $S^+(i)$ and $S^-(i)$, respectively. ($S^+(0)$ is the signal returned from the area the radar is attempting to image.)

One must also note that the signal strength computed in (23) is infinite at $\theta_l = 0$, an unphysical result arising from the implicit assumption that the range resolution is smaller

than the area subtended by the beamwidth—this assumption breaks down as $\theta_l \to 0$. In order to avoid this, we cut off the calculation at one-half the range-beamwidth.

Azimuth Ambiguities

The azimuth ambiguity sidelobe ratio (AASR) is computed from:

$$\text{AASR} = \frac{\sum_{m \neq 0} \int_{-B_D}^{B_D} G^2(f + m f_p) \, \mathrm{d}f}{\int_{-B_D}^{B_D} G^2(f) \, \mathrm{d}f} \tag{30}$$

where B_D is the Doppler Bandwidth for processing (100 Hz), f_p is the PRF, and G is the gain of the antenna. We can re-write the Doppler frequency, $f = f(\phi)$, where ϕ is the azimuth angle, using $f = \frac{2v}{\lambda} \sin \phi$. Thus, (30) can be rewritten:

$$\text{AASR} = \frac{\sum_{m=m_{\min}, m \neq 0}^{m_{\max}} \int_{\sin^{-1}\left[\frac{\lambda}{2v}(m f_p - B_D/2)\right]}^{\sin^{-1}\left[\frac{\lambda}{2v}(m f_p + B_D/2)\right]} G^2(\phi) \cos \phi \, \mathrm{d}\phi}{\int_{-\sin^{-1}\frac{\lambda B_D}{4v}}^{\sin^{-1}\frac{\lambda B_D}{4v}} G^2(\phi) \cos \phi \, \mathrm{d}\phi} \tag{31}$$

where

$$m_{\min} = -\left(\frac{2v}{\lambda} - \frac{B_D}{2}\right)\frac{1}{f_p} \tag{32}$$

and $m_{\max} = -m_{\min}$. Thus we just integrate over the azimuth gain pattern of the antenna.

ISLR

Presently, the Integrated Side-Lobe Response is not computed, but is assumed as an input parameter. Its value is -15 dB of the signal strength.

Quantization Noise

The quantization noise is computed from a model which assumes that the error made is random. Thus, the error across a range of values for which only one quantized value is available is linear with the distance from the quantized value. This error is integrated to obtain the quantization error. In addition, there is error due to saturation which occurs when the signal exceeds the maximum quantum value. Thus, there is some optimum value for the saturation threshhold, for a given number of quantization bits and a given signal strength, such that the sum of the saturation error and the quantization error is minimized. This level has been computed for various numbers of bits in a very clear and concise paper. A table of the total error introduced when this optimal saturation threshhold has been used is reproduced here and in the system performance software, Table 5, and has been used to compute the quantization noise for this system. For example, with 4 bits for each (real) sample and a signal level of -130.372 dB at the boresight, the corresponding quantization noise level is -149.267 dB.

Bits Per Sample	Noise Factor
3	0.0465
4	0.0129
5	0.0037
6	0.00105
7	0.00031
8	0.000089
9	0.000025
10	0.000007

Table 5: Quantization noise table. See text for assumptions made in generating this table. The value in the right column is multiplied by the signal level to obtain the quantization noise for the number of bits in the left column.